

Navier-Stokes Module

TECHNISCHE UNIVERSITÄT BERLIN

Institut für Strömungsmechanik
und Technische Akustik

Müller-Breslau-Str. 15
10623 Berlin

Last updated: September 21, 2018

Author: Julius Reiss, Philipp Krah, Mario Sroka

Abstract

In this article we summarize validations, implementations and benchmarks of the compressible Navier-Stokes equations in skew symmetric form using adaptive grids.

Contents

1	Implementations	2
1.1	2D/3D compressible Navier-Stokes Equations	2
1.2	Penalized Navier Stokes Equations	2
1.3	Bogey-Cacqueray-Bailly Filter	3
2	Validations	7
2.1	Sods Shock Tube	7
2.2	Volume Penalization	8
3	Performance Benchmarks	16

1 Implementations

In this section we give some details describing the implementation of the Navier-Stokes module. An overview of the module is given on the last page of this section.

1.1 2D/3D compressible Navier-Stokes Equations

The compressible Navier-Stokes equations rewritten in skew symmetric form [1] in 2D/3D cartesian coordinates read, $(\alpha, \beta = 1, 2, 3)$

Continuity equation

$$\partial_t \sqrt{\rho} = -\frac{1}{2\sqrt{\rho}} \partial_\alpha (\rho u_\alpha), \quad (1)$$

Navier-Stokes equations

$$\partial_t (\sqrt{\rho} u_\alpha) = -\frac{1}{2\sqrt{\rho}} [u_\alpha \partial_\beta (\rho u_\beta) + u_\beta \partial_\beta (\rho u_\alpha)] - \frac{1}{\sqrt{\rho}} \partial_\beta \tau_{\alpha\beta} + \frac{1}{\sqrt{\rho}} \partial_\alpha p, \quad (2)$$

Energy conservation equation

$$\partial_t p = -\gamma \partial_\beta (u_\beta p) + (\gamma - 1)(u_\alpha \partial_\alpha p) + (\gamma - 1) [\partial_\alpha (u_\beta \tau_{\alpha\beta} + \phi_\alpha) - u_\alpha \partial_\beta \tau_{\alpha\beta}]. \quad (3)$$

The right hand side (RHS) is implemented in the files `RHS_2D_navier_stokes.f90` and `RHS_3D_navier_stokes.f90`.

1.2 Penalized Navier Stokes Equations

Speaking in terms of IBVP with differential operator L and initial value $q(\vec{x}, t_0) = q_0$ on Ω , the set of equations changes in the following way:

$$\begin{cases} \partial_t q = L(q), & \vec{x} \in \Omega \\ q(\vec{x}, t) = q_{\text{ref}}, & \vec{x} \in \partial\Omega_s \end{cases} \xrightarrow{\text{penalized}} \partial_t q = L(q) - \underbrace{\frac{\chi_{\Omega_s}}{C} (q - q_{\text{ref}})}_{\text{penalization term}}. \quad (4)$$

Here we have omitted additional boundary conditions on $\partial\Omega$. The geometry of Ω_s is represented by the mask function χ_{Ω_s} , with value $\chi_{\Omega_s} = 1$ inside and $\chi_{\Omega_s} = 0$ outside Ω_s (see fig. 1). Thus, in the area Ω_p , where $\chi_{\Omega_s} = 0$, one recovers the unpenalized system. Whereas in Ω_s the system is penalized for values q which differ from the reference value q_{ref} . The strength of the penalization is given by the constant $0 < C \ll 1$. Because inside Ω_s the system is forced to penalization terms break of the domain is called physical domain Ω_p because all penalization terms in eqs. (5) to (7) vanish.

Following [2, 3], compressible Navier-Stokes equations in skew symmetric form eqs. (1) to (3) are modified by the penalization terms marked in bold font:

$$\partial_t \sqrt{\rho} = -\frac{1}{2\sqrt{\rho}} \partial_\alpha (\rho u_\alpha) - \frac{1}{2\sqrt{\rho}} \frac{\chi_{\text{Sp}}}{C_{\text{Sp}}} (\rho - \rho^{\text{Sp}}), \quad (5)$$

$$\begin{aligned} \partial_t (\sqrt{\rho} u_\alpha) = & -\frac{1}{2\sqrt{\rho}} [(u_\alpha \partial_\beta (\rho u_\beta) + u_\beta \rho \partial_\beta u_\alpha)] - \frac{1}{\sqrt{\rho}} \partial_\beta \tau_{\alpha\beta} - \frac{1}{\sqrt{\rho}} \partial_\alpha p \\ & - \frac{1}{\sqrt{\rho}} \frac{\chi_{\text{Sp}}}{C_{\text{Sp}}} (\rho u_\alpha - \rho^{\text{Sp}} u_\alpha^{\text{Sp}}) - \frac{\chi_\eta}{\sqrt{\rho} C_\eta} (\rho u_\alpha), \end{aligned} \quad (6)$$

$$\begin{aligned} \partial_t p = & -\gamma \partial_\beta (u_\beta p) + (\gamma - 1)(u_\alpha \partial_\alpha p) + (\gamma - 1) [\partial_\alpha (u_\beta \tau_{\alpha\beta} + \phi_\alpha) - u_\alpha \partial_\beta \tau_{\alpha\beta}] \\ & - \frac{\chi_{\text{Sp}}}{C_{\text{Sp}}} (p - p^{\text{Sp}}) - \frac{\chi_\eta}{C_\eta} (p - \rho R_s T_0). \end{aligned} \quad (7)$$

1.3 Bogey-Cacqueray-Bailly Filter

Implemented as in [4] use the form:

$$\begin{aligned} q_i \mapsto q_i - \left(\sigma_{i+\frac{1}{2}} Dq_{i+\frac{1}{2}} - \sigma_{i-\frac{1}{2}} Dq_{i-\frac{1}{2}} \right) \\ \text{with } \sigma_{i\pm\frac{1}{2}} = \frac{\sigma_{i\pm 1} + \sigma_i}{2} \quad \text{and} \quad Dq_{i+\frac{1}{2}} = \sum_{j=1-n}^n c_j q_{i+j} \end{aligned} \quad (8)$$

and:

$$c_1 = -0.210383 \quad c_2 = 0.039617 \quad (9)$$

In the first step we compute the filtering magnitude $D\hat{f}_i$ at each grid point $x_i \in \Omega_h$

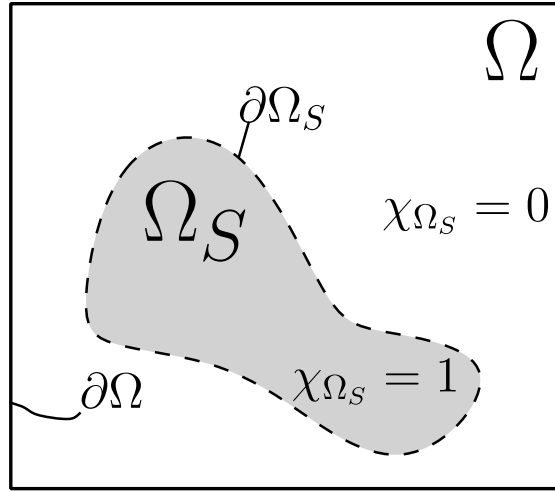


Figure 1: Computational domain Ω with obstacles Ω_s . The gray color indicates the region of the obstacle and its boundary $\partial\Omega_s$ is drawn with a dashed line.

from the dilatation $f = \text{div } \vec{u}$ using a second order filter

$$Df_i = \frac{-f_{i+1} + 2f_i - f_{i-1}}{4}, \quad (10)$$

$$D\hat{f}_i = \frac{1}{2}[(Df_i - Df_{i+1})^2 + (Df_i - Df_{i-1})^2]. \quad (11)$$

The filtering magnitude is then normalized to the local speed of sound $c_i = \gamma p_i / \rho_i$

$$r_i = \frac{D\hat{f}_i}{c_i^2 / \Delta x^2} \quad (12)$$

and can be used as a shock sensor. If the local shock sensor reaches a certain threshold (normally $r_{\text{th}} \equiv 10^{-5}$) the filtering strength should be $\sigma_i > 0$, therefore [4] uses the function

$$\sigma_i = \frac{1}{2} \left(1 - \frac{r_{\text{th}}}{r_i} + \left| 1 - \frac{r_{\text{th}}}{r_i} \right| \right). \quad (13)$$

For smoother transitions we use instead

$$\sigma_i = 1 - \tanh \left(\frac{r_{\text{th}}}{7r_i} \right). \quad (14)$$

After the computation of σ_i the state vector is filtered by applying the filter eq. (8) to the state vector in conservative form $(\rho, \rho u_1, \rho u_2, E)$ with total energie $E = p/(\gamma - 1) + 1/2 \rho \vec{u}^2$ at every lattice side i . As seen in fig. 2 the filter is only applied locally where $\sigma > 0$. Because we use the dilatation as filtering indicator, only discontinuities in the velocity components are detected by the shock capturing filter. Nevertheless, this also removes the oscillations of all other components of the state vector plotted in figs. 3b and 4b. It is also important to note that the transition in the right sponge domain (see fig. 3b) does not trigger the filter.

In fig. 4 the advantage of the shock capturing filter is clearly demonstrated. The explicit filters in fig. 4a show large oscillations at the discontinuities, while the shock capturing filter preserves the form of the internal energy $e = p(\gamma - 1)/\rho$ with much less oscillations.

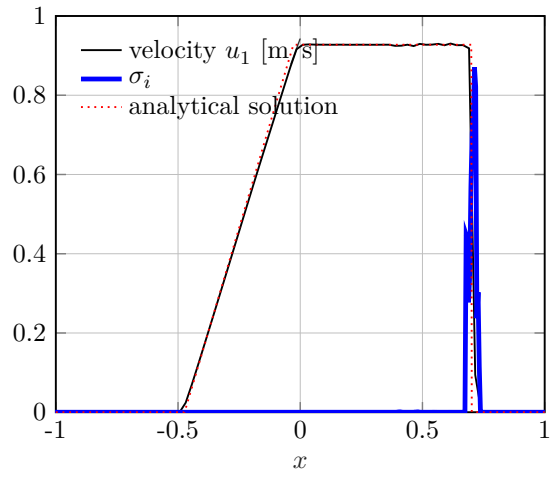
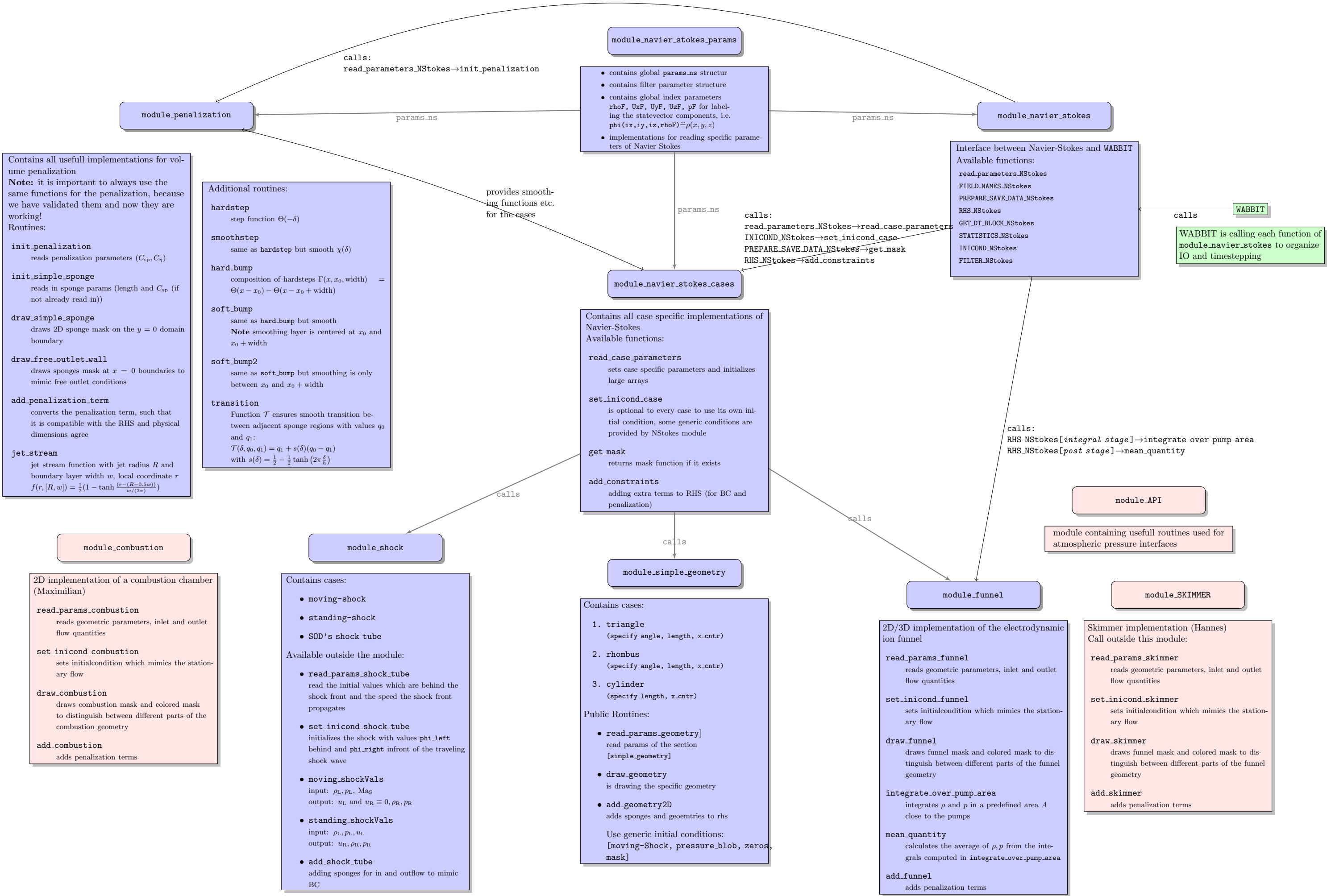


Figure 2: Filtering strength σ_i computed from the dilatation. Example for the velocity of *Sod's shock tube*, with analytical solution (dashed line) and numerical solution (continuous line) at time $t = 0.4$.



2 Validations

2.1 Sod's Shock Tube

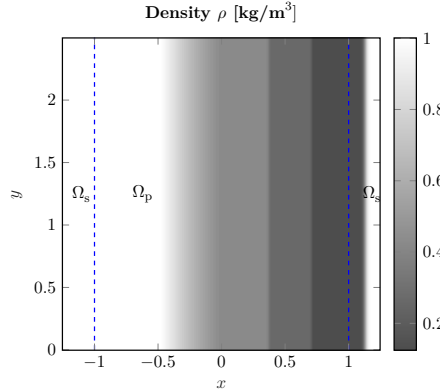
To optimize the parameters of the filter and verify the chosen solver for $\mu = 0$ (Euler equations), we carry out a test case: *Sod's shock tube* [5]. For our solver the test case was generalized to two dimensions $\Omega = [-1.25, 1.25] \times [0, 2.5]$. The implemented initial conditions for $(x, y) \in \Omega$ read:

$$(\rho, u, v, p) |_{t=0} = \begin{cases} (\rho_L, u_L, v_L, p_L) & \text{for } x \leq 0, \\ (\rho_R, u_R, v_R, p_R) & \text{for } x > 0. \end{cases} \quad (15)$$

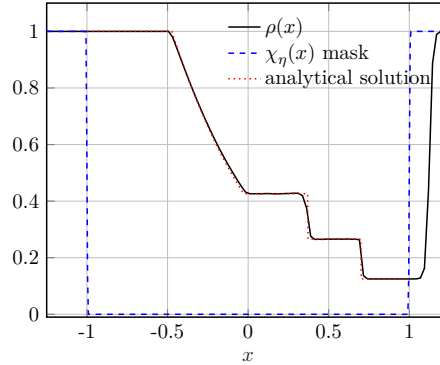
Here we use the values suggested by [5]

$$q_L = \begin{pmatrix} \rho_L \\ u_L \\ v_L \\ p_L \end{pmatrix} = \begin{pmatrix} 1.0 \\ 0.0 \\ 0.0 \\ 1.0 \end{pmatrix}, \quad q_R = \begin{pmatrix} \rho_R \\ u_R \\ v_R \\ p_R \end{pmatrix} = \begin{pmatrix} 0.125 \\ 0.0 \\ 0.0 \\ 0.1 \end{pmatrix}. \quad (16)$$

The total two-dimensional domain $\Omega = \Omega_p \cup \Omega_s$ is shown in fig. 3a. For the two-dimensional shock tube we use periodic boundary conditions in the y -direction and Dirichlet boundary conditions in the x -direction. The Dirichlet conditions are implemented using sponge terms at both sides $-1.25 < x < -1$ and $1 < x < 1.25$, with the corresponding values of eq. (16) and $C_{SP} = 0.001$. Smooth transitions between left and right boundary values are parametrized with the transition function $\mathcal{T}(x, q_L, q_R)$ (??). As seen in fig. 3b the transition is centered at $x_0 = 1.125$ in the right sponge domain.



(a) Image plot of the density ρ . The --- line separates physical domain $\Omega_p = (-1, 1) \times [0, 2.5)$ from the non physical domain $\Omega_s = \Omega \setminus \Omega_p$.



(b) Numerical solution $\rho(x, y)$ at line $y = 1.25$ compared to the analytical solution.

Figure 3: Density plot of *Sod's shock tube* for $t = 0.4$ s in the full simulation domain $\Omega = [-1.25, 1.25] \times [0, 2.5)$. Computed with shock capturing filter in every time step.

In addition to fig. 3a, we show the one dimensional profile of density $\rho(x, y, t)$, internal energy $e(x, y, t)$, and velocity $u_1(x, y, t)$ at line $y = 1.25$ and $t = 0.4$ in figs. 2, 3b and 4b. In all cases the numerical solution shows excellent agreement with the analytical solution. This test case shows that we are able to capture shocks with our method and validates the implementation of the compressible Navier-Stokes equations in the frictionless case.

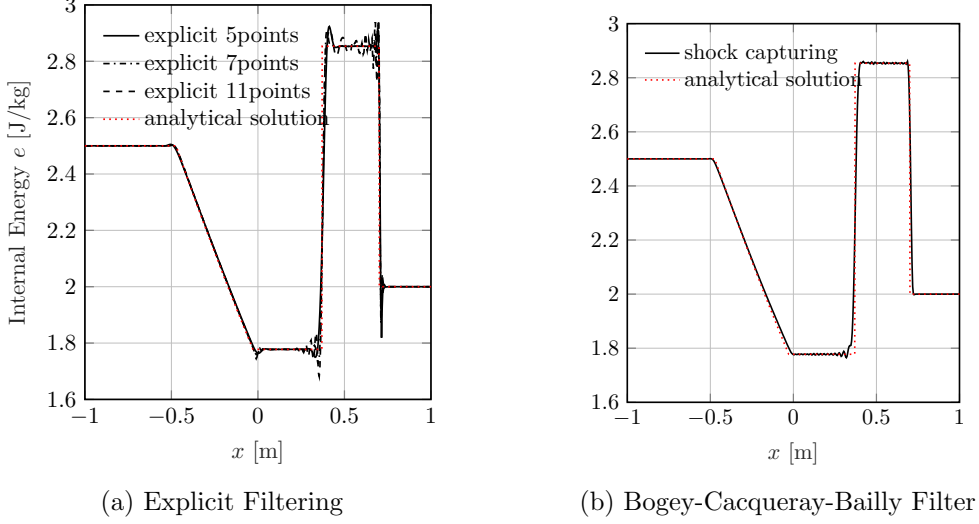


Figure 4: Analytical vs. numerical solution of *Sod's shock tube* [5] at $t = 0.4$. Comparison between explicit filter (fig. 4a) and shock capturing filter (fig. 4b) applied to the numerical solution in every time step. The plotted quantity is the internal energy $e = p(\gamma - 1)/\rho$.

2.2 Volume Penalization

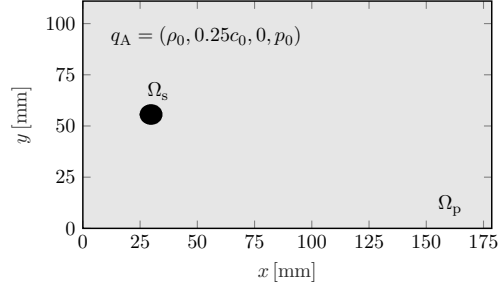
Test case A: The vortex street for low Mach number $Ma = 0.25$, $Re = 185$ flow.

The scenario is illustrated in fig. 5a. We consider a homogeneous flow in x -direction characterized by the free stream inflow with state-vector q_A . After sufficiently long time, instabilities in the flow will lead to swirling vortices at the backside of the cylinder, known as vortex-shedding. An image of the vorticity $\omega_z = \partial_1 u_2 - \partial_2 u_1$ in fig. 6, shows the vortex pairs swirling in opposite directions at time $t^* = tc_0/l_0 = 1200$. The vortex-shedding leads to periodic oscillatory lift and drag forces acting on the sphere [2]:

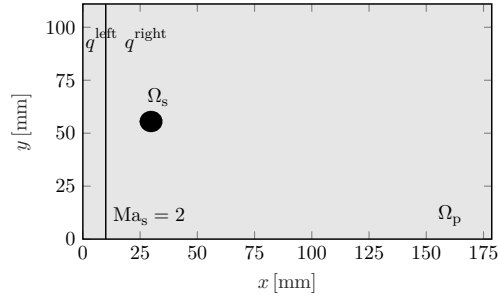
$$\vec{F}_{\Omega_s} = \frac{1}{C_\eta} \int_{\Omega} \chi_\eta(\rho \vec{u}) \nabla, \quad (17)$$

which can be used to analyse our implementation. We analyse $\vec{F}_{\Omega_s} = (F_1, F_2)$ with help of the dimensionless drag and lift coefficients:

$$C_D = \frac{F_1}{\frac{1}{2} \rho_A u_{A,1}^2 l_0} \quad \text{and} \quad C_L = \frac{F_2}{\frac{1}{2} \rho_A u_{A,1}^2 l_0}, \quad (18)$$



(a) Image of test case A. The cylinder is centered at $(x_0, y_0) = (0.03, 0.0555)$ m. The flow streams with $\text{Ma} = 0.25$, $\text{Re} = 185$ from left to right with q_A at the inlet at $x = 0.0$ mm.



(b) Image of test case B and C. The cylinder is centered at $(x_0, y_0) = (0.03, 0.0555)$ m. A shock wave is moving with $\text{Ma}_s = 2$ from left to right. The black line at $x = 0.1L_x$ is the initial shock front. The values to the left and right of the shock front are q^{left} , q^{right} .

Figure 5: Test case scenario for the stream around a cylinder for low Reynolds number $\text{Re} = 185$. Periodic boundary conditions are applied in all directions of the computational domain. Inlet and outlet flow is set by the sponge area for all points (x, y) with $x > 0.9L_x$.

in fig. 7. Figure 7a shows the time evolution of both coefficients. After $t^* = 500$ the coefficients reach a state of steady oscillation. The frequency f_0 of this oscillation can be determined by a Fourier transformation of the oscillation, shown in fig. 7b. In order to relate f_0 to results in the literature, we use the dimensionless form, called Strouhal number:

$$\text{ST} = \frac{f_0 l_0}{u_{A,1}}. \quad (19)$$

Table 1 compares the Strouhal number, the root mean square of the lift coefficient $\widehat{C_L}$ and the mean of the drag coefficient $\overline{C_D}$ to results of the literature.

	$\overline{C_D}$	$\widehat{C_L}$	ST
Khalili et. al [6]	1.282	0.431	0.191
Lu et. al [7]	1.31	0.422	0.195
Guilmineau et. al [8]	1.287	0.443	0.195
Liu et. al [9]	1.289	0.451	0.197
Experimental results [8]	1.28		0.19
average	1.29(1)	0.44(1)	0.194(3)
present study $C_\eta = 10^{-5}$	1.955	0.310	0.192
present study $C_\eta = 10^{-8}$	1.280	0.486	0.194

Table 1: Comparison of the drag coefficients eq. (18) and Strouhal number eq. (19). For the present study $(J_{\max}, B_s) = (4, 33)$.

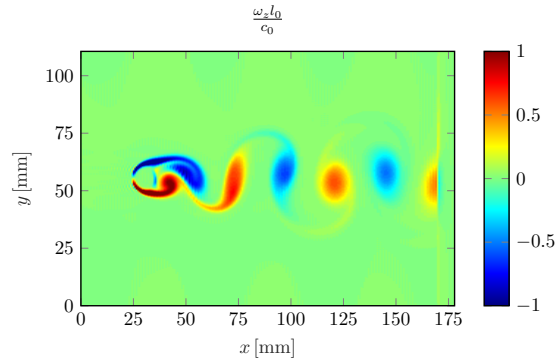
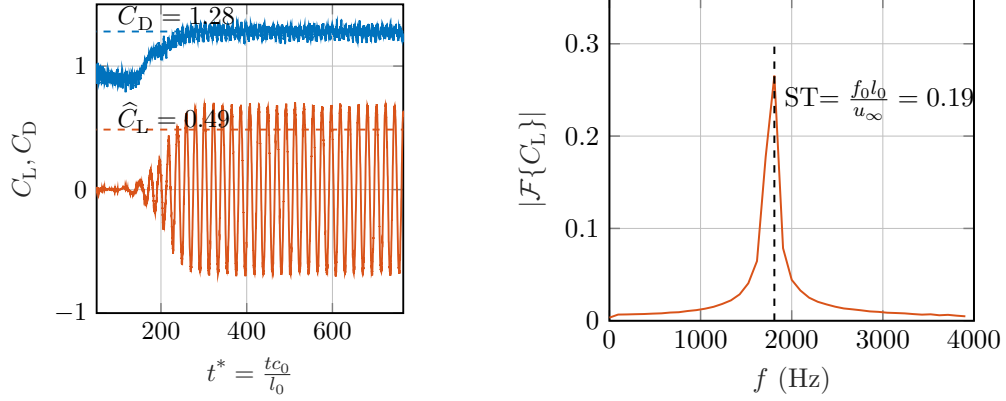


Figure 6: Test case A - Vorticity scaled by the speed of sound c_0 at time $t^* = tc_0/l_0 = 1200$. Oscillating vortices occur after sufficient large simulation time.

Test case B: A Mach-2 shock wave (speed of the wave front $\text{Ma}_s = 2$) interacting with the cylinder.



(a) Drag and lift coefficients C_D , C_L plotted over time. The upper line corresponds to the drag coefficient and the lower line to the lift coefficient. Dashed lines represent mean and root mean square value of the coefficients

(b) Fourier transform of C_L for $t^* \geq 600$. The Strouhal number ST is obtained from the vortex-shedding frequency f_0 with highest Fourier amplitude $|\mathcal{F}\{C_L\}|$

Figure 7: Test case A - lift and drag of the vortex street.

The initial shock configuration,

$$q(\vec{x}, 0) = \begin{cases} q_B^{\text{left}} = (\rho_0, u_{\text{left}}, 0, p_0) & \text{for } x < 0.1L_x \\ q_B^{\text{right}} = (\rho_{\text{right}}, 0, 0, p_{\text{right}}) & \text{otherwise} \end{cases} \quad (20)$$

is illustrated in fig. 5b, where the values $u_{\text{left}}, \rho_{\text{right}}, p_{\text{right}}$ are calculated from ρ_0, p_0 and Ma_s using the Rankin–Hugoniot conditions (see [10] p. 98 ff). The shock wave is traveling with $Ma_s = 2$ from left to right hitting the cylinder. For this test case, we perform numerical simulations at $(J_{\text{max}}, B_s) = (3, 33)$ using different penalization parameters C_η , to probe the convergence of the solution inside the penalized volume Ω_s . We evolve the solution to $t = 2 \cdot 10^{-4} \text{ s}$, where the shock wave has passed the cylinder. From this point, we calculate the relative penalization errors:

$$\|\vec{u}\|_{L_2(\Omega_s)} := \frac{1}{u_{\text{max}}} \left(\int_{\Omega} \chi_\eta \|\vec{u}(x, y)\|^2 \, \text{xy} \right)^{1/2}, \quad (21)$$

$$\|p - \rho T_{\Omega_s} R_s\|_{L_2(\Omega_s)} := \frac{1}{p_{\text{max}}} \left(\int_{\Omega} \chi_\eta |p(x, y) - \rho(x, y) T_{\Omega_s} R_s|^2 \, \text{xy} \right)^{1/2}, \quad (22)$$

with $u_{\text{max}}, p_{\text{max}}$ the maximal pressure and velocity norm in Ω_p . Figure 8 shows the convergence of the relative errors inside Ω_s for $10^{-8} \text{ s} \leq C_\eta \leq 10^{-5} \text{ s}$. We estimate convergence rates of $\mathcal{O}(C_\eta^{0.8})$, which is less than the ones reported by [2], but still higher than the theoretical convergence rate predicted by [11] for the incompressible case. In fig. 9 we show the profiles of all quantities along the line $0 < x < 150 \text{ mm}$, $y = L_y/2$ for various C_η . All quantities show a significant drop at the shock front $x \approx 90 \text{ mm}$

independently of C_η . Another drop is located in the penalized area. Here the depth depends on the penalization parameter C_η . One should note that the density inside a solid body is not penalized by the set of eqs. (5) to (7), which is necessary for conservation of mass. However, since the reference velocity inside the penalization area is set to zero, $\partial_t \rho = 0$ for $C_\eta \rightarrow 0$ and therefore ρ should stay constant. We observe in fig. 9b that this is only achieved when $C_\eta = 10^{-8}$ s.

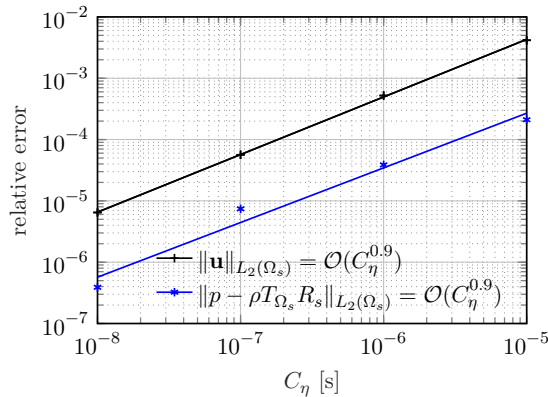


Figure 8: Test case B -Relative error of the velocity norm (eq. (21)) and pressure (eq. (22)) inside the cylinder.

Test case D: Comparison of shock angles for high Mach flow around triangles.

Next, we consider an inlet gas flow with $\text{Ma} = 2$ around isosceles triangles with half angle $\theta = 10^\circ, 20^\circ$, shown in fig. 10. From inviscid flow theory a straight shock front is predicted, which detaches from the triangle. The predicted angle β between a horizontal line and the shock front, is computed implicitly by solving

$$\tan \theta = 2 \cot \beta \left[\frac{\text{Ma}^2 \sin^2 \beta - 1}{\text{Ma}^2 (\gamma + \cos 2\beta) + 2} \right]. \quad (23)$$

for a given half angle θ . Tables 2 and 3 show the theoretical predictions and measured shock angles of our simulations. The shock angle is computed from the blue lines fitted to the right apex of the shock, shown in figs. 10a and 10b. For all configurations, we choose the same inlet flow at the inlet boundary $x = 0$ mm. The inlet flow values are identical to the ion funnel simulation, except for the pressure, which is set to $p_{\text{in}} = 21756.0$ Pa to obtain $c_{\text{sound}} = \sqrt{\gamma p_{\text{in}} / \rho_{\text{in}}}$, such that $\text{Ma} = u_{\text{in}} / c_{\text{sound}} = 2$.

Test case E: Shock front for high Mach flows around a cylinder.

For the last test case, we compute the flow around a cylinder with radius $r = 10$ mm, shown in fig. 11. The inlet flow quantities are identical to test case D ($\text{Ma} = 2$). Following [2] we measure the distance Δ between the shock front and the obstacle on the stagnation line $y = L_y/2$. The distance from the shock front has been experimentally measured and a theoretical description of the hyperbola shaped shock front is given in

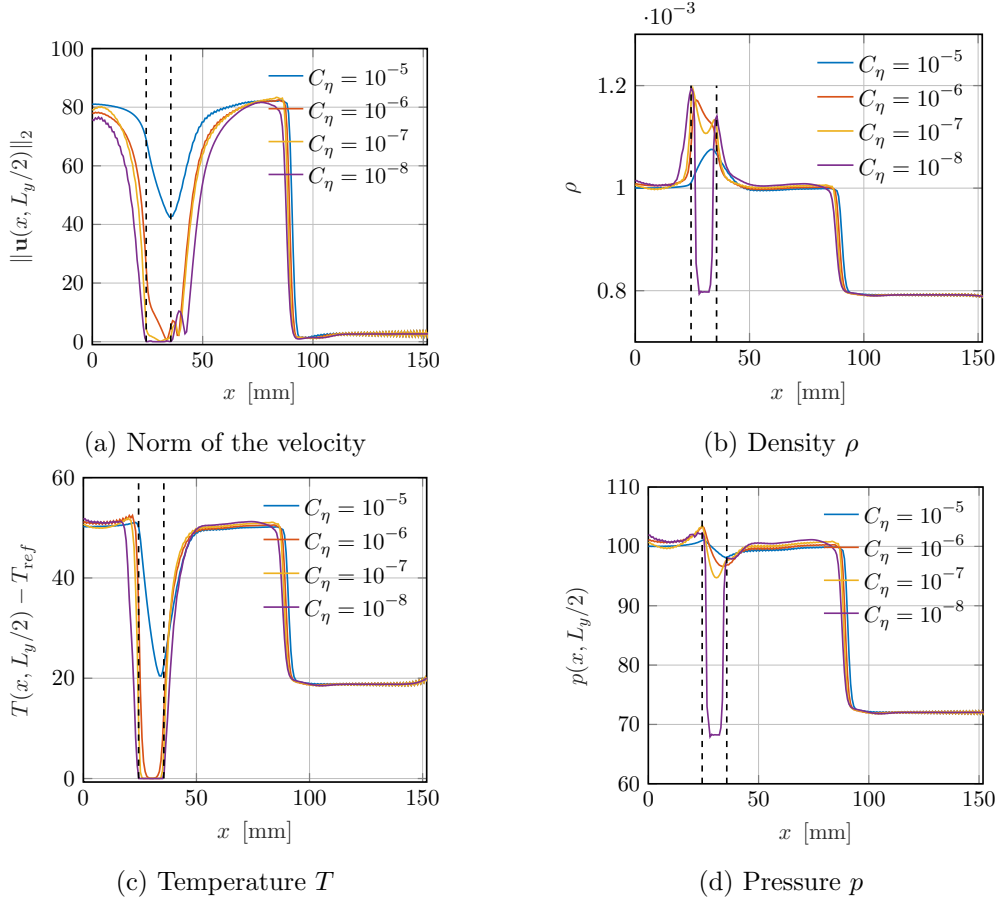
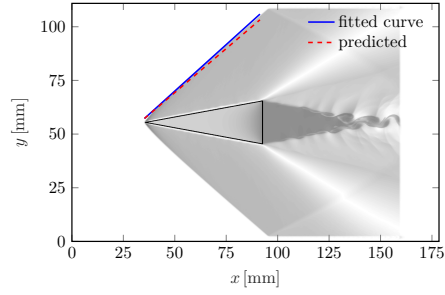


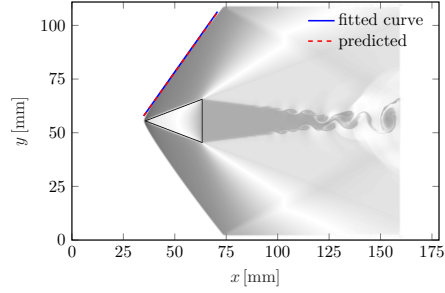
Figure 9: Test case B - Penalization error at $t = 2 \cdot 10^{-4}$ of a high Mach shock wave hitting the cylinder. The shock front has reached $x \approx 0.09$ mm. All four quantities of the state vector are plotted along the line $0 < x < 150$ mm, $y = L_y/2$. The penalized area is in between the dashed lines, forcing the state vector to its reference values.

	$J_{\max} = 3$	$J_{\max} = 4$	$J_{\max} = 5$
$C_\eta = 10^{-5}$ s	53.45°	52.01°	51.38°
$C_\eta = 10^{-6}$ s	56.87°	54.75°	53.56°
$C_\eta = 10^{-7}$ s	60.51°	56.74°	54.49°
$C_\eta = 10^{-8}$ s	64.31°	59.44°	56.61°

Table 2: Test case D - Comparison of shock angles for half angle $\theta = 20^\circ$ and $B_s = 33$. The theoretical predicted angle is $\beta = 53.4229^\circ$.



(a) $\theta = 10^\circ$, $C_\eta = 10^{-6}$ s, $J_{\max} = 5$



(b) $\theta = 20^\circ$, $C_\eta = 10^{-6}$ s, $J_{\max} = 5$

Figure 10: Test case D - Schlieren image of the density ρ for flow angles $\theta = 10^\circ, 20^\circ$, with $J_{\max} = 5$, $B_s = 33$ and $t = 5 \cdot 10^{-4}$ s. The blue lines at the right apex are used to compute the shock angle. The red line shows the theoretical prediction.

	$J_{\max} = 3$	$J_{\max} = 4$	$J_{\max} = 5$
$C_\eta = 10^{-5}$ s	44.96°	42.99°	41.83°
$C_\eta = 10^{-6}$ s	45.90°	42.70°	40.90°
$C_\eta = 10^{-7}$ s	49.78°	44.01°	41.04°
$C_\eta = 10^{-8}$ s	55.26°	47.33°	43.16°

Table 3: Test case D - Comparison of shock angles for half angle $\theta = 10^\circ$ and $B_s = 33$. The theoretical predicted angle is $\beta = 39.3139^\circ$.

equation (1) of [12]. The theoretical stagnation line with distance Δ is the horizontal line plotted in fig. 11. Additionally, we plot the hyperbolic shock shape using equation (1) of [12] with free stream Mach angle ($\arcsin(1/\text{Ma}) = 30^\circ$). An analysis of the shock front distance Δ was performed using various values of C_η and J_{\max} . The resulting Δ/r values are compared to the predicted value $\Delta/r = 1.24$ in table 4. The best result is obtained for $C_\eta = 10^{-6}$ s and $J_{\max} = 5$.

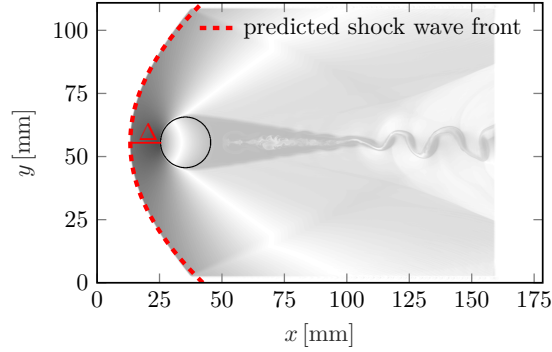


Figure 11: Test case E - Density shock wave predicted by [12] with free stream Mach angle 30° compared to the simulation $J_{\max} = 5$, $C_\eta = 10^{-6}$ s.

	$J_{\max} = 3$	$J_{\max} = 4$	$J_{\max} = 5$
$C_\eta = 10^{-5}$ s	1.1254	0.9608	0.9140
$C_\eta = 10^{-6}$ s	1.4705	1.3161	1.2421
$C_\eta = 10^{-7}$ s	1.8357	1.4877	1.3085
$C_\eta = 10^{-8}$ s	2.4155	1.8305	1.4664

Table 4: Comparison of shock detachment Δ/r for penalization parameter C_η and grid points $N = 32 \cdot 2^{J_{\max}}$. From experimental fitted data [12] the predicted value for $\text{Ma} = 2$ is $\Delta/r = 1.24$. The radius of the cylinder is $r = 10$ mm.

3 Performance Benchmarks

References

- [1] Julius Reiss and Jörn Sesterhenn. A conservative, skew-symmetric finite difference scheme for the compressible NavierStokes equations. *Computers & Fluids*, 101:208 – 219, 2014.
- [2] O. Boiron, G. Chiavassa, and R. Donat. A high-resolution penalization method for large Mach number flows in the presence of obstacles. *Computers & Fluids*, 38(3):703 – 714, 2009.
- [3] Laurent Bernier. Raumladungseffekte von ionengeladenen Gasströmungen durch Kapillaren, 7 2014.
- [4] Christophe Bogey, Nicolas de Cacqueray, and Christophe Bailly. A shock-capturing methodology based on adaptative spatial filtering for high-order non-linear computations. *Journal of Computational Physics*, 228(5):1447 – 1465, 2009.
- [5] Gary A Sod. A survey of several finite difference methods for systems of nonlinear hyperbolic conservation laws. *Journal of Computational Physics*, 27(1):1 – 31, 1978.
- [6] M. Ehsan Khalili, Martin Larsson, and Bernhard Mller. Immersed boundary method for viscous compressible flows around moving bodies. *Computers & Fluids*, 170:77 – 92, 2018.
- [7] X.-Y. Lu and C. Dalton. Calculation of the timing of vortex formation from an oscillating cylinder. *Journal of Fluids and Structures*, 10(5):527 – 541, 1996.
- [8] E. Guilmineau and P. Queutey. A numerical simulation of vortex shedding from an oscillating circular cylinder. *Journal of Fluids and Structures*, 16(6):773 – 794, 2002.
- [9] Cheng Liu and Changhong Hu. An efficient immersed boundary treatment for complex moving object. *Journal of Computational Physics*, 274:654 – 680, 2014.
- [10] Eleuterio F Toro. *Riemann solvers and numerical methods for fluid dynamics: a practical introduction*. Springer-Verlag Berlin Heidelberg, 2. edition, 1999.
- [11] Philippe Angot, Charles-Henri Bruneau, and Pierre Fabrie. A penalization method to take into account obstacles in incompressible viscous flows. *Numerische Mathematik*, 81(4):497–520, 1999.
- [12] Frederick S Billig. Shock-wave shapes around spherical-and cylindrical-nosed bodies. *Journal of Spacecraft and Rockets*, 4(6):822–823, 1967.